FULL PAPER

Printed Electronics

ADVANCED
FUNCTIONAL
MATERIALS

www.afm-journal.de

Paper with Power: Engraving 2D Materials on 3D Structures for Printed, High-Performance, Binder-Free, and All-Solid-State Supercapacitors

Tengyuan Zhang, Xia Li, Eaton Asher, Sixu Deng, Xueliang Sun, and Jun Yang*

The prevalence of the Internet of Things (IoT) and wearable electronics create an unprecedented demand for new power sources which are low cost, high performance, and flexible in many application settings. In this paper, a strategy for the scalable fabrication of high-performance, all-solid-state supercapacitors (SCs) is demonstrated using conventional paper and an inkjet printer. Emerging printed electronics technology and low-cost chemical engraving methods are bridged for the first time to construct Cu_xO nanosheets, in situ, on the 3D metallized fiber structures. Benefitting from both the "2D Materials on 3D Structures" design and the binder-free nature of the fabricated electrodes, substantial improvements to electrical conductivity, aerial capacitance, and electrochemical performance of the resulting SCs are observed. With the proposed strategy, the fabricated SCs can be seamlessly integrated into any printed circuit, sensors, or artwork; the properties of these SCs can be easily tuned by simple pattern design, fulfilling the increasing demand of highly customized power systems in the IoT and flexible/wearable electronics industries.

1. Introduction

The rapid development of the Internet of Things (IoT) and wearable electronics has accelerated the insatiable demand for low-cost energy storage systems capable of seamlessly integrating with their intended applications.[1–3] Electrochemical capacitors, also known as supercapacitors (SCs), have been the subject of intense study due to their superior power density, longer cycle life, and unparalleled charge–discharge speed when compared to conventional batteries and traditional capacitors.[4–7] According to the energy storage mechanism, SCs can be categorized into electrochemical double-layer capacitor and pseudocapacitor types. To achieve high-power/ energy density in a pseudocapacitor, high-specific surface area, high electrical conductivity, and rapid ion diffusion paths are necessary. Research has shown ruthenium oxides/hydroxides to exhibit the desired high pseudo-charge capacitance as an active electrode material, however, the high cost for such materials greatly hinders its wide applications.[8,9] Other transition metal oxides, such as MnO_2, Cu_xO, NiO, Co_3O_4, and VO_x, have each been meticulously studied in hopes of providing a cheaper, equally efficient alternative.[10–20] Of the above-mentioned metal oxides, Cu_xO was considered to be particularly promising due to its low cost, relatively high theoretical capacity, proven safety, and abundance as a natural resource.

Traditional SCs usually contain sheet-type electrodes, liquid electrolytes, and separator membranes as its core components. These elements are most commonly fabricated through a stacking or winding process. However, such traditional assembly of components greatly limits the capacitor's flexibility, as well as variety of form factors. Recent advances in material sciences and printed electronics technology have started to overcome these challenges, offering a variety of power sources, such as thin-film batteries and all-printed SCs.[21–24] These next-generation power sources show performance comparable to existing techniques, yet are foldable, bendable, and even stretchable.[22,25,26] In the conventional fabrication process of a printed SC, the electrochemical active materials are directly printed onto the substrate, adhering to the current collectors by simple physical absorption.[21,27,28] Though this may simplify the fabrication process, the electrode materials will quickly flake off from the current collector due to the weak adhesion and great volume changes during charging/discharging processes, causing poor cycling life and large capacity loss. One solution to this issue is to incorporate the binding agent; in a more traditional electrode, a polymer binder usually plays the role of integrating electroactive particles onto the supporting materials and/or current collectors. A caveat to adding these insulating and electrochemically inactive polymer binders is, it will increase the inner resistance of the assembly which will inevitably offset the gained improvements to the SC's performance. Furthermore, the extra manufacturing process will greatly reduce the cost-efficiency, which is of critical importance for the booming IoT and wearable electronics industry, where trillions of low-cost energy storage systems are demanded every year.[1] One promising strategy to fabricate a bind-free nanostructured electrode is to grow the electrochemical active materials directly on the current collectors. In recent years, nanostructured copper oxide/hydroxide for energy storage applications has been deposited onto current collectors in a

Dr. T. Zhang, Dr. X. Li, E. Asher, Dr. S. Deng, Prof. X. Sun, Prof. J. Yang
University of Western Ontario
London, Ontario N6A 3K7, Canada
E-mail: jyang@eng.uwo.ca

variety of methods including electrodeposition, hydrothermal synthesis, chemical vapor deposition, chemical bath deposition, as well as dry and wet oxidization.[29–33] Among these methods, wet oxidization is considered to be one of the simplest and the least expensive way to fabricate nanostructured copper oxide/hydroxide on current collectors-on a large scale without requiring harsh experimental conditions and toxic chemicals. However, regular printed copper circuits based on copper nanomaterials cannot survive the wet chemical oxidation (engraving) process because the nano-sized copper will quickly get oxidized and lost most or all of its conductivity before any formation of the nanostructured copper oxide and/or hydroxide, hindering the emerging printed electronics technology from taking advantage of this method to create highly customized flexible power sources with various form factors. As a result, the wet chemical methods have only been successfully demonstrated on bulk copper/metal products (such as copper foil, copper tape, and copper wire) to generate nanostructured copper oxide.[34–38] For example, Shinde et al. synthesized CuO nanoflowers on copper foil, showing a specific capacitance of ≈ 498 F g^{-1} at 5 mV s^{-1}[35]; Dubal et al. deposited CuO nanosheets onto stainless steel plate, showing a specific capacitance of 43 F g^{-1} at 10 mV s^{-1}[36]; Endut et al. synthesized vertical CuO nanoflakes on copper foil with a specific capacitance of 190 F g^{-1} at 5 mV s^{-1}.[38] The limitation is that the synthesised electrochemical active materials would only exist on the surface of the substrate, which would result in limited ion/electron transfer paths and very little active material available per specific area to contribute to the performance of the SCs. It is therefore urgent to develop a facile and effective strategy to take full advantages of both the emerging printed electronics technology, and low-cost wet chemical oxidation method for the large-scale fabrication of high-performance, binder-free nanostructured electrode with various form factors and flexibility.

To address all challenges mentioned above, we propose and demonstrate a strategy for low-cost scalable fabrication of all-solid-state flexible and high-performance SC with binder-free 3D porous Cu$_x$O nanosheets on regular cellulose paper using an inkjet printer. For the first time, we bridge the emerging printed electronics technology and low-temperature chemical engraving method together with electroless copper deposition, to fabricate high-performance porous current collectors in a large scale on regular paper with a superior electrical conductivity of 0.005 Ω sq^{-1}, on which porous Cu$_x$O nanosheets are engraved in situ to construct the binder-free 3D flexible electrodes. Taking advantages of the micro porous structure formed by randomly orientated cellulose fibers, the engraved Cu$_x$O nanostructures present on every metallized fiber, creating a ≈ 90 μm thick 3D electrode with hierarchical micro-nanostructures. Thanks to the binder-free design and high electrochemical active materials loading per specific area, the printed planar SC shows low inner resistance of only ≈ 0.3 Ω and high areal specific capacitance of 384.2 mF cm^{-2} at a scanning speed of 10 mV s^{-1}. It is also worth mentioning that this simple low-cost method repeatedly produced SCs with good cycling stability, achieving $\approx 80\%$ capacity retention after 10 000 cycles with no post-production alterations. With the adoption of the printed electronics technology, the printed SCs can be monolithically integrated with paper substrate and seamlessly embedded into

any printed circuits on paper, adding a new dimension to the printed devices for applications in IoT and wearable electronics. As a proof of concept, all-solid-state flexible planarly SCs arrays are fabricated on paper to power a light-emitting diode (LED) and the SCs array are also seamlessly integrated into printed circuits and word arts, demonstrating the endless potential of the proposed strategy.

2. Results and Discussion

2.1. Fabrication Process

Fabricating highly conductive current collectors on cellulose paper is challenging. The paper substrate may look smooth and orderly to the naked eye, but it is in fact made of a highly complex network of randomly orientated cellulose fibers. The porous property of these fibers enables them to absorb conductive inks (e.g., silver and copper nanoparticles) into them, instead of leaving them on the surface, preventing the nanomaterials inside the ink from touching with each other, resulting in low conductivity. Furthermore, conductive copper traces printed with nanomaterials are incompatible with the simple and low-cost chemical engraving method for synthesize of nanostructured copper oxide due to the significant conductivity loss during the engraving process. Other in situ synthesis methods, mentioned previously, each suffer from one or more prohibitive drawbacks. Whether it is the requirement of special equipment, harsh chemicals, excessive energy consumption, or complicated fabrication processes, each new 'solution' to this problem faces its own self-defeating limitation which makes commercial low-cost scalable production impractical.

To overcome these challenges, we adopt the electroless metal deposition (ELD) technique as a bridge to combine the printed electronics and chemical engraving together for low-cost large-scale fabrication of 3D nanostructured electrode. The ELD technique relies on an autocatalytic redox reaction to deposit metals on a catalyst-preloaded substrate, offers a low-cost way to fabricate metallized substrate with properties closed to bulk metal.[39,40] However, untreated cellulose paper substrate struggle with capturing catalyst ions due to lack of binding sites, resulting in severe resolution loss and poor adhesion between deposited metal and substrate during the printing process.[41,42] Untreated cellulose paper does not readily accept catalyst ions during the ELD process due to a lack of binding sites. Attempting to do so results in very poor ELCD resolution and subsequently leads to a failure of adhesion between the deposited metal and substrate.[41] Thus, one of the key step in the proposed approach is to modify the cellulose paper with a special developed coating. Poly (4-vinylpyridine) (P4VP) has been used in the past to modify substrates, allowing them to uptake silver ions. It achieves this through its strong ability to chelate with transitional metal ions.[43,44] P4VP polymers can be directly coated onto substrate by physical absorption, however, these coating will eventually come off during the long-time emersion in acrylic solution for chemical engraving. Epoxy groups have been observed to form strong covalent bonds with the hydroxyl groups found on cellulose paper. This, combined with the fact that it also cross-links with the pyridine groups found

in P4VP molecules, makes SU-8 a great candidate for use as an intermediary between P4VP and the cellulose substrate. Meanwhile, the highly reactive epoxy groups can also form strong covalent bonds with the abundant hydroxyl groups presenting on each cellulose fiber. Thanks to these properties, epoxy can be used as a bridge to graft P4VP molecules onto cellulose fibers, achieving a strong chemical bonding with the substrate which can withstand the long-time chemical engraving process. Thus, in this work, P4VP and SU-8 were employed as the main coating components for the surface modification of cellulose paper. **Figure 1** shows the proposed fabrication method of making high-performance 3D Cu_xO nanostructured electrodes on regular paper.

The coating solution was prepared by dissolving SU-8, P4VP, and a small amount of polyvinylpyrolidone into a mixture of 2-propanol and 1,4-dioxane. The solution was then applied to the substrate by immersing the pre-cut cellulose paper in the solution for 5 s. The sample was then baked in an oven at 130 °C for 15 min to introduce covalent bonding between SU-8, P4VP, and the paper's cellulose fibers. The resulting substrate will have abundant pyridine ligands along each fiber (Figure 1b), which are necessary to capture catalyst silver ions in the subsequent step. Attributed to the ring-opening reaction of epoxide groups, the dominant bonding type of the coating will be carbon–oxygen bonds, which are highly resistant to

alkali solutions and allow the treated substrate to withstand the following ELD and chemical engraving process–both of which involve alkali solutions. Next, silver ions were deposited onto selected areas (planar SCs pattern in this case) through inkjet printing (Figure 1c). When the silver nitrate contacts the primed paper substrate, the nitrogen atom in the unoccupied pyridine group, will capture the silver ions to form strong coordination bonds. These chemical bonds ensure a much more resistant link between the substrate and P4VP than that achieved through simple physical absorption. As mentioned prior, this physical resilience is important for the deposition of copper. Such chemical bonds keep the printed silver ions firmly attached to the surface of each cellulose fiber, enhancing the adhesion between substrate and copper generated in the following ELCD process (Figure 1f).

The unique fiber-based porous structure of the cellulose paper allows the ink to penetrate through to a certain depth, creating a 3D catalyst-loaded area which significantly increases the number of available targets for copper deposition. Thanks to this phenomenon, cellulose fibers not only get metallized on the very top surface, but also inside the substrate, creating a 3D porous metallized area with a thickness of ≈90 µm. Details of this process can be found in the Experimental Section. In the following chemical engraving process, the selectively metallized paper was immersed in NaOH solution for 48 h, as
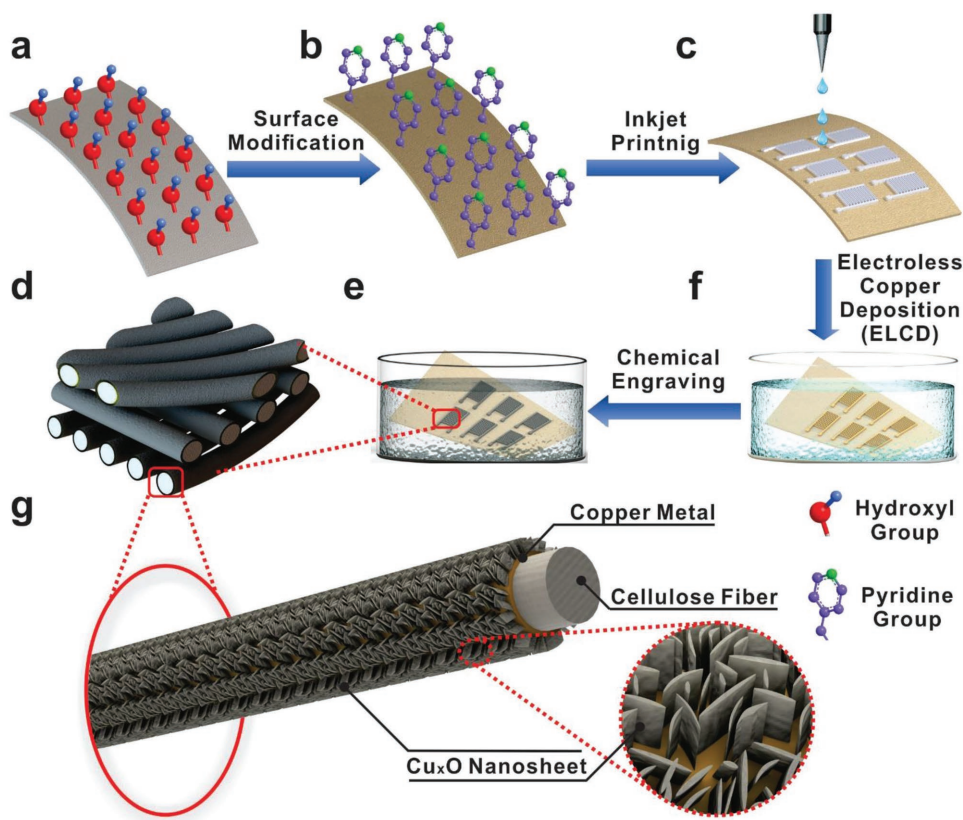

Figure 1. Fabrication process of binder-free 3D Cu_xO nanostructure on cellulose paper. a) Surface of cellulose paper with large amount of hydroxyl groups. b) The substrate present abundant pyridine groups after surface modification. c) Inkjet printing of planar SC. d) Microstructure of the sample after chemical engraving. e) Chemical engraving of the selectively metallized substrate. f) Electroless copper deposition for the metallization of catalyst-activated area. g) A single cellulose fiber after chemical engraving with binder-free nanostructured active materials.

**ADVANCED
SCIENCE NEWS**
www.advancedsciencenews.com

**ADVANCED
FUNCTIONAL
MATERIALS**
www.afm-journal.de

depicted in Figure 1e. Under basic solution conditions in the presence of oxygen, the copper metal was gradually oxidized, giving rise to $Cu_xO/Cu(OH)_2$ arrays along the surface of each metallized cellulose fiber. After vacuum dry at 85 °C, most of the copper hydroxide was converted to copper oxide, revealing the Cu_xO nanosheets produced in situ along each metallized fiber. Figure 1d shows the microstructure of the sample after chemical engraving. Each fiber is covered by a layer of Cu_xO nanosheet arrays, which are shown to be black in the picture. The chemically engraved fibers orientate randomly to form a porous 3D structure, greatly increasing the concentration of electrochemically active materials per unit area. Figure 1g gives a more detailed look of a single cellulose fiber after chemical engraving, with binder-free nanostructure of active materials. As depicted a layer of copper metal, shown in the color orange, tightly wraps around the cellulose fiber (gray in color). Vast amounts of vertically oriented Cu_xO nanosheets are present on the surface, providing a high flux of ions and fast conducting pathways for electrons throughout the electrodes. This also provides ample space for Cu_xO nanosheets to accommodate the strain of volume change during the charge/discharge process, allowing the device to remain high performance and good flexibility with longer cycling life. Furthermore, thanks to the facile process and the absence of special equipment, high-quality Cu_xO nanosheet arrays of this kind can be fabricated at a large scale at low cost. Moreover, as the Cu_xO nanosheet arrays are grown in situ by the direct engraving of metallized cellulose fibers, the printed patterns can be used immediately—without further modifications—as flexible electrodes for SCs. The absence of polymer binder improves the conductivity and eliminates the concern of polymer swelling, as has been observed in some cases, enhancing the structural and cycling stability as well as the electrochemical performance of the assembled SCs.

2.2. Characterization of Morphology

Figure 2a shows the picture of the same sample after ELCD (up) and after chemical engraving (down). The color of the electrodes changes from dark-yellow to black after the chemical engraving process, indicating the formation of copper oxide layer. Though the chemical engraving process introduces $Cu(OH)_2$ on the surface, which typically presents itself as blue in color, the sample appears pure black. We hypothesize this to be caused by the nanostructured $Cu(OH)_2$ nanosheets, which absorb most of the incident light making the surface appear to be black. The microstructure of the engraved sample was investigated using field emission scanning electron microscopy (FE-SEM), the result of which is presented in Figure 2b–d. Figure 2b shows the surface morphology of the sample, depicting the randomly oriented metallized cellulose fibers, with different diameters, forming a porous 3D microstructure. Figure 2c shows a cross-sectional image of the sample post-chemical engraving. The presence of copper/copper oxide underneath the surface can be
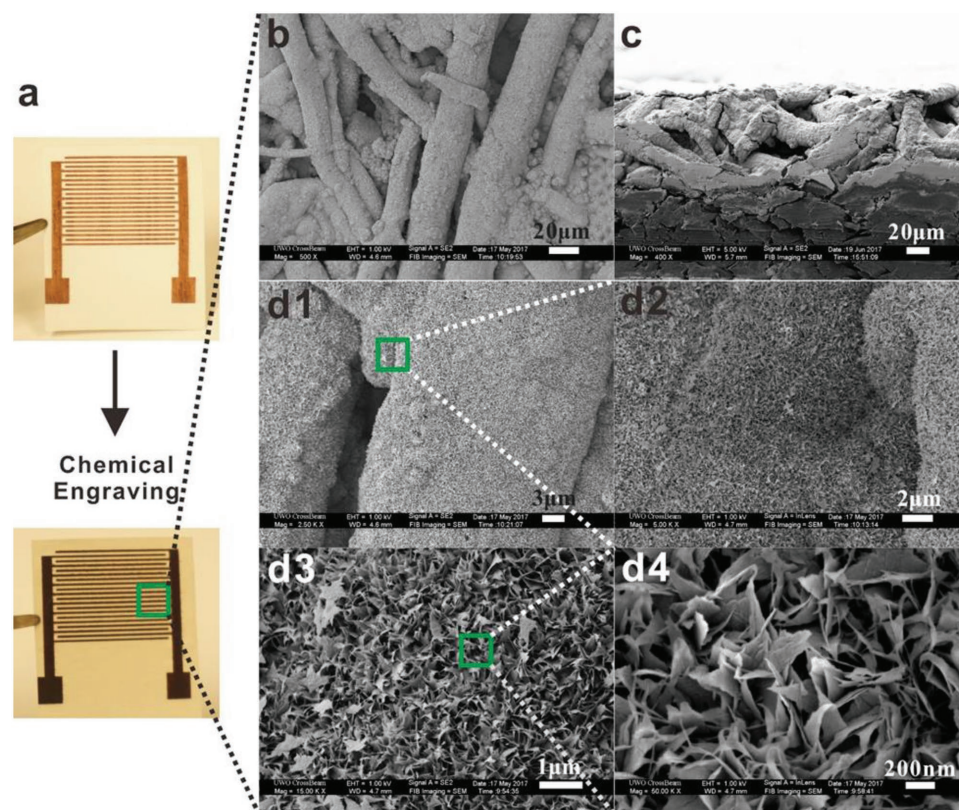

Figure 2. a) Optical images of samples after electroless copper deposition (up) and after chemical engraving (down). SEM images of b) surface morphology and c) cross-section of the chemical engraved sample. d) SEM images taken using magnifications of 2.5 K (d1), 5 K (d2), 10 K(d3), and 50 K(d4), respectively to reveal the hierarchical micro-nanostructures of the post-engraved samples.

**ADVANCED
SCIENCE NEWS**
www.advancedsciencenews.com

**ADVANCED
FUNCTIONAL
MATERIALS**
www.afm-journal.de

seen to a depth of around 90 µm, indicating that the ink had penetrated 90 µm below the surface and generate a 3D metallized volume after ELCD. FE-SEM images with increasing magnification were taken to further reveal the nanostructure on the surface of each fibers (Figure 2d1–d4). Figure 2d1–d4 was taken using magnifications of 2.5, 5, 10, and 50 K, respectively. Both the microstructure, formed by cellulose fibers, and nanostructure, formed by Cu_xO nanosheets, can be clearly seen in Figure 2d1. Figure 2d2 shows the magnified area of d1, wherein dense, uniform, homogeneous arrays of these nanosheet arrays can be clearly identified. The nanosheet layer conforms to the surface of the cellulose fibers with predominantly vertical orientation. Under greater magnification (Figure 2d3,d4), we can see that the nanosheets are several nanometers thick and cross with each other in a variety of different angles. This has left a highly porous nanostructure with adequate space between each other to accommodate the volume change during the charge/discharge process. It is known that different growth rates of the crystal faces determine the final morphology of the nanomaterials.[45] The dominated facet plane of the copper generated through electroless deposition is (111), which faces outwards and has the highest density.[39–42] According to the Bravais–Friedel–Donnay–Harker law, the growth rate of orthorhombic $Cu(OH)_2$ crystal is proportional to $1/d_{hkl}$.[46–48] Thus, in this work, the growth rate of $Cu(OH)_2$ on (111) facet (pointing outwards along each metallized cellulose fiber) is much faster than those along the other directions, leading to the formation of vertical aligned nanosheets. After dehydration in the vacuum chamber, most $Cu(OH)_2$ converted to Cu_xO, and preserved the morphology of the $Cu(OH)_2$ precursor. It is also worth mentioning that the concentration of NaOH in the chemical engraving solution had a significant effect on the surface morphology of the nanostructures. We observed that lower NaOH concentrations (<30 mg mL^{-1}) resulted in a flower-like nanostructure, while higher NaOH concentrations (>50 mg mL^{-1}) resulted in a coral-like nanostructure. The chemical–electrical performance of all three of these nanostructures were investigated, and it was found that samples displaying the currently presented morphology of nanosheet arrays showed far superior performance to the others. The required concentration of NaOH in the

solution need to be controlled at ≈40 mg mL^{-1} for the generation nanosheet arrays shown in Figure 2b–d.

2.3. Conductivity Test

Conductivity of the electrode is critical to the performance of the final assembled device; lower levels of resistance greatly reduce the power lost to inefficiency, and also minimizes the drop in available voltage during the charging/discharging process. Maximizing the conductivity of electrodes, where possible, will result in greater the performance of the SCs. In a regular printed electronics fabrication process, the electrode is produced by the direct inkjet printing of conductive inks. As the conductive properties are, in this case, entirely dependent on the ink's scarcely applied particles, this process results in a relatively high level of resistance within the circuit and thus not ideal for most applications. In comparison, during the ELCD process adopted in this work, the source of conductive material (copper) is from the electroless plating bath. When the autocatalytic reaction is triggered by the printed silver ion, copper begins growing on the catalyst-activated (i.e., printed) areas and will continue to do so until it is removed from the solution. The thickness of the deposited copper layer can be precisely controlled by manipulating the time in which the substrate resides in the solution.[39,42,49] Because this layer thickness in turn determines the conductivity of the substrate, it is reasonable to predict that the conductivity of the printed electrodes can be precisely controlled by altering the time of their residence in the ELCD solution. The change in each sheet's resistance as a function of ELCD processing time was investigated using the conventional four-probe method. The resistance was measured at 15-min intervals, and the conductivity of the sample was calculated according to the value of measured sheet resistance and metallization depth. This was used to further reveal the intrinsic electrical properties of the materials. These results are summarized in **Figure 3**a.

According to these results, the sheet resistance of the printed electrodes steadily decreases during the ELCD process, which corresponds to the progressive formation of connection between
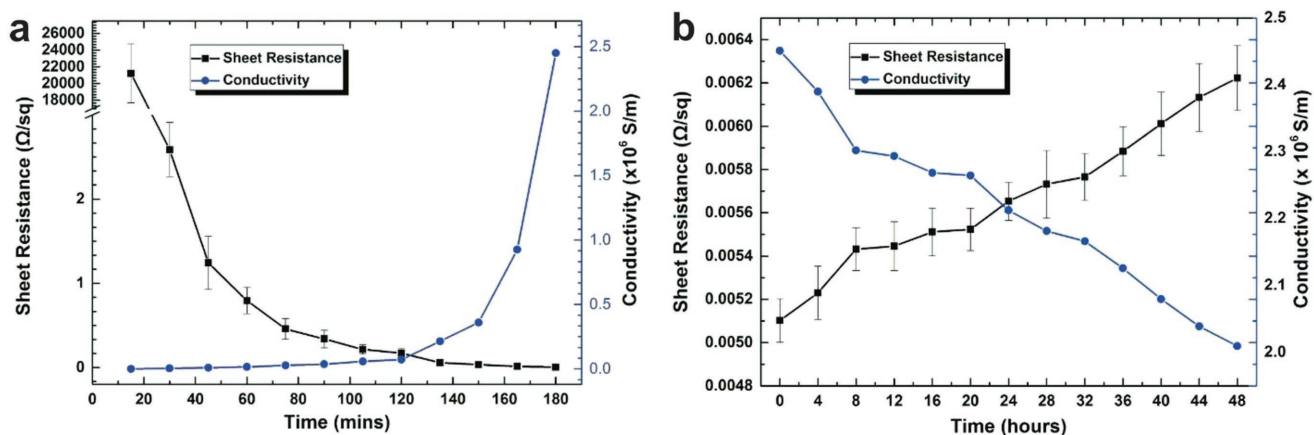

Figure 3. a) Graph showing the change of sheet resistance and its equivalent conductivity with different electroless copper plating time ranging from 0 to 180 min. b) Graph showing the sheet resistance and equivalent conductivity change of samples with 3 h electroless copper plating time over a 48 h period of chemical engraving.

copper grains and the increased thickness of the copper layer. After 180 mines (3 h) of electroless copper plating, samples displayed a sheet resistance of ≈5.2 mΩ sq^{-1}—which is much better than that of the electrodes fabricated by direct printing of conductive inks (≈50 mΩ sq^{-1}). The conductivity of these samples at this point is roughly 2.45×10^6 S m^{-1}, which is about 24 times lower than that of bulk copper (59.6×10^6 S m^{-1}). These results are reasonable due to the existence of cellulose fiber inside the deposited copper and high porosity of the copper-fiber conductive structure. ELCD process shows promise to provide ultra-low sheet resistance in electrodes that has been difficult to achieve by direct printing of conductive inks. It is worth mentioning that the conductivity of these electrodes can be further enhanced by increasing the ELCD residence time. Although this is an attractive quality for circuits, it was not utilized for the present study because of its inherent trade-offs: any increases to the density of the generated copper will result in corresponding decreases to the space between cellulose fibers, which an important factor to consider when fabricating SCs. Through trial and error, we determined that an ELCD duration of approximately 3 h led to a nice balance between electrode conductivity and porosity, and the best SC performance, motivating us to use this as the standard ELCD residence time for all electrodes utilized in this work. Recognizing that the chemical engraving process is in fact a kind of oxidization process, we were concerned that there may be undesired losses in conductivity due to copper oxidization. Hence, the relationship between sheet resistance/conductivity and chemical engraving time was investigated. Figure 3b shows the sheet resistance/conductivity change of samples with 3 h electroless plating time over a 48 h period of chemical engraving. Data were collected every 4 h using the same four-probe measurement station. The resistance of samples increases at a near-constant rate of about 0.46% per hour from the beginning (≈5.1 mΩ sq^{-1}), to its final value (≈6.2 mΩ sq^{-1}) attained after 48 h. This increase in sheet resistance, totaling 22% throughout the entire process, can be attributed to the oxidization of the metallized cellulose fibers. In summary, the chemical engraving process does in fact introduce a conductivity loss of ≈22%, but when that is held in context to its exceptionally low initial sheet resistance, the loss in conductivity is minimal and has little appreciable impact on its ability to be used in high-performance devices.

2.4. Electrochemical Properties

Symmetric planar SCs-with as-prepared, binder-free electrodes-were assembled using KOH–PVA gel as the solid-state electrolyte. The cyclic voltammetry (CV) studies were performed to analyze the electrochemical behavior of the assembled device using a two-electrode setup with potential ranging from 0 to 0.6 V at different scan rate of 10, 20, 40, 80, 100, and 200 mV s^{-1} respectively. All electrochemical tests were configured as a two-electrode system. The results are shown in **Figure 4**a. Each CV curve consists of a pair of strong redox peaks which are attributed to the Cu^{2+}/Cu$^+$ and Cu$^+$/Cu^{2+} transition, revealing the pseudo-capacitance behavior of the electrodes.[20,35] It is further noted that when the scan rate increases, the shape of the CV curve changes. The cathodic peaks show right shift

to high voltages, while the anodic peaks shift to lower values at higher scan rate. To reveal more about the electrochemical capacitive performance of the electrode, galvanostatic charge–discharge was measured at various current densities and a voltage window of 0–0.6 V (Figure 4b). None of the resulting six curves exhibit the ideal triangular shape, whose deviance suggests contribution from the redox reaction of Cu$^+$/Cu^{2+} as shown in the CV curves. The initial drop in voltage whilst discharging the SCs can be attributed to the internal resistance of the assembled device. The inner resistance comes from the electrode, electrolyte, and the interfaces between them. For this work, longer ELCD time will greatly reduce the resistance of the electrode, however, as discussed before, the porosity of the electrode will also be reduced due to longer growth of copper, resulting in loss of performance in other aspects such as cycling life and specific capacitance. Adopting an electrolyte with higher ionic conductivity will also reduce the inner resistance, which will in turn reduce the voltage drop during discharging process. Both the capacitance per unit area and the capacitance per gram at different scanning rate were calculated according to the CV curves, area of the electrodes, and the total mass of the active materials on the electrodes. The total mass of the active materials was determined by measuring the difference in weight before and after washing the sample in 1 M HCl solution. The results are shown in Figure 4c,d, respectively. The specific capacitance of these samples was found to decrease as scan rate was increased. This is to be expected, as ions passed at lower current densities can penetrate deeper into the 3D structure of the electrode material, providing them access to a greater number of pores; at higher current densities, utilization of electrode material was limited to only the outer surface of electrodes. At a scan rate of 5 mV s^{-1}, the material exhibited its highest specific capacitance of 384.2 mF cm^{-2} (Figure 4c) and 537.8 F g^{-1} (Figure 4d). To evaluate the rate capability of the SC, we calculated its specific capacitance at different discharging current density according to the galvanostatic charge/discharge results (Figure 4b). At 1 mA cm^{-2}, the device was able to deliver a specific capacitance of 523.2 F g^{-1}, while at the highest current density (20 mA cm^{-2}), the value dropped to 266.5 F g^{-1}. In between, we got 433.71, 373.4, 343.1, and 313.4 F g^{-1} corresponding to current density 2, 4, 8, and 10 mA cm^{-2}, respectively. It is worth mentioning that, other researchers have investigated the supercapacitive properties of nanostructured, binder-free Cu$_x$O electrodes.[34–38] Unlike the presented work however, these electrodes were produced on non-porous copper tape or foil where electrochemical active Cu$_x$O grew only on the top surface, limiting its aerial capacitance in a great extent. In this work, taking advantages of the microporous structure of paper, the loading of Cu$_x$O expand from a 2D surface to a 3D architecture of cellulose fibers, resulting in boosted specific capacitance. Moreover, the 3D nanostructured architecture provides a fast, ionic transportation path, contributing to the improved performance as well. To the best knowledge of the authors, the aerial capacitance of the presented samples exceeds those of all other Cu$_x$O electrodes produced by any means of printing.

To determine if the proposed technology is robust enough to withstand the endless number of charge–recharge cycles demanded by industry, the printed capacitors' cycling
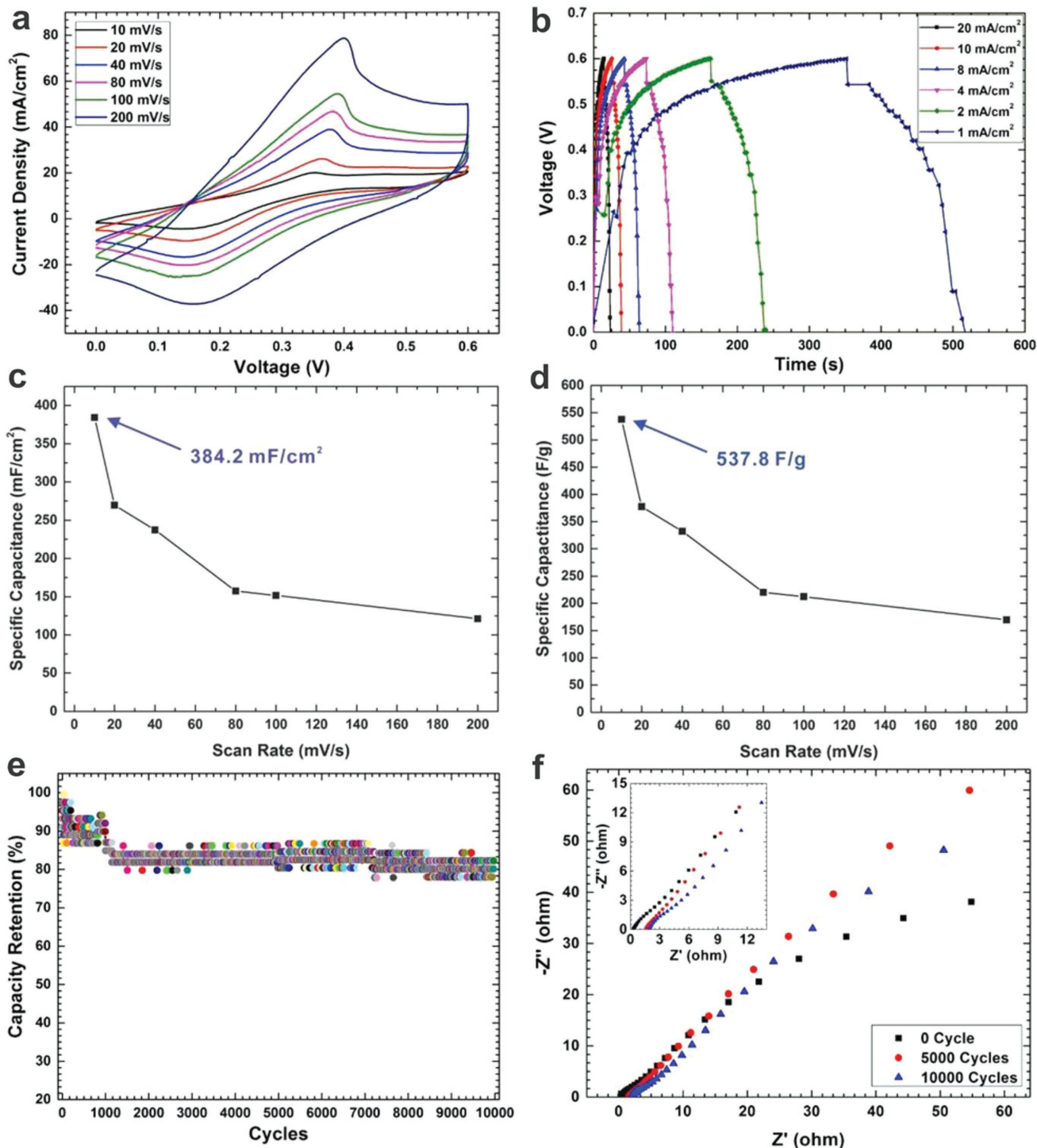
Figure 4. Graphs showing a) CV curves at different scan rate of 10, 20, 40, 80, 100, and 200 mV s^{-1} respectively, b) galvanostatic charge/discharge profiles with different current density of 1, 2, 4, 8, 10, and 20 mA cm^{-2}, c) specific capacitance versus area, d) mass, e) capacity retention as a function of cycle number with current density of 20 mA cm^{-2}, and f) Nyquist plots collected at open circuit potential of the as-prepared SCs.

performance was investigated with voltage window of 0–0.6 V. Capacitance retention as a function of cycle number was explored using the charge–discharge curves at the highest current density (20 mA cm^{-2}; Figure 4e). As illustrated, a sharp decrease in specific capacity can be observed during the first

few hundred cycles, leveling out to roughly 85% of its initial capacity by cycle 1000. The loss of specific capacity may result from ineffective contacts between part of the unstable Cu$_x$O nanosheets and the metallized fibers. After 1000 cycles, the slope evens out, lose only 3% capacitance over the subsequent

9000 cycles (Figure 4e), showing stable cycling performance thanks to the advanced micro-nano hierarchical structures and strong adhesion between the engraved Cu$_x$O and current collectors. The observed loss of capacitance is believed to have resulted from a combination of collapsed Cu$_x$O nanosheets, ineffective electrode–electrolyte contacts, and deteriorated ionic transfer pathways. Electrochemical impedance test (EIS) was conducted at open circuit potential in the frequency range from 0.01 Hz to 100 kHz, to further show the properties of the as-prepared devices. The Nyquist plots were created for samples having underwent 0, 5000, and 10 000 charge/discharge cycles (see Figure 4f). It can be seen that all three samples displayed similar shapes in both high-frequency (semicircle) and low-frequency (linear) circuit potentials. The shifted intercept of impedance, down the real axis at high frequencies, reflects the equivalent series resistance (ESR) of the device. This is closely related to the electrolytic resistance, the intrinsic electrical resistance of the Cu$_x$O nanostructured layers, as well as the contact resistance between electrolyte, electrodes, and current collectors. The ESR values of the three tested samples were 0.27, 1.56, and 1.90 Ω, corresponding to samples having undergone 0, 5000, and 10 000 charging/discharging cycles, respectively. The resistance to charge transfer (RCT) can be estimated from the Nyquist plot using the diameters of the semicircles plotted along the real (x) axis. The devices' RCT increases as a function of cycle number, reflecting the large

initial drop in specific capacitance followed by the leveling out after the first few hundred cycles, confirming the findings in the cycling tests. In brief, the EIS shows similar value during the whole cycling tests, especially between 5000 and 10 000 cycles, indicating good stability of the engraved nanostructures.

2.5. XPS and XRD Characterization

X-ray photoelectron spectroscopy (XPS) was used initially to determine out the precise species of copper present on the surface of the samples. XPS survey spectra of samples both before and after chemical engraving process are shown in **Figure 5** a,b, respectively. In the sample analysed prior to chemical engraving (left), the high-resolution Cu 2p scanning captured a strong peak of 932.6 eV (Figure 5a1), suggesting the presence of Cu metal, Cu(I) oxide, or more likely, a mixture of both. It is difficult to confidently ascertain which copper species is present here due to the close proximity between characteristic peaks of Cu metal (932.6 eV) and Cu(I) oxide (932.7 eV). Cu LMM was scanned to further identify the copper species on the surface. The Cu LMM spectrum, shown in Figure 5a2, reveals two distinct peaks, 916.8 and 918.6 eV, which can be ascribed to Cu(I) oxide and Cu metal, respectively, implying the presence of both Cu$_2$O and Cu metal on the surface. By calculating the integral area of the two peaks, the relative proportions of
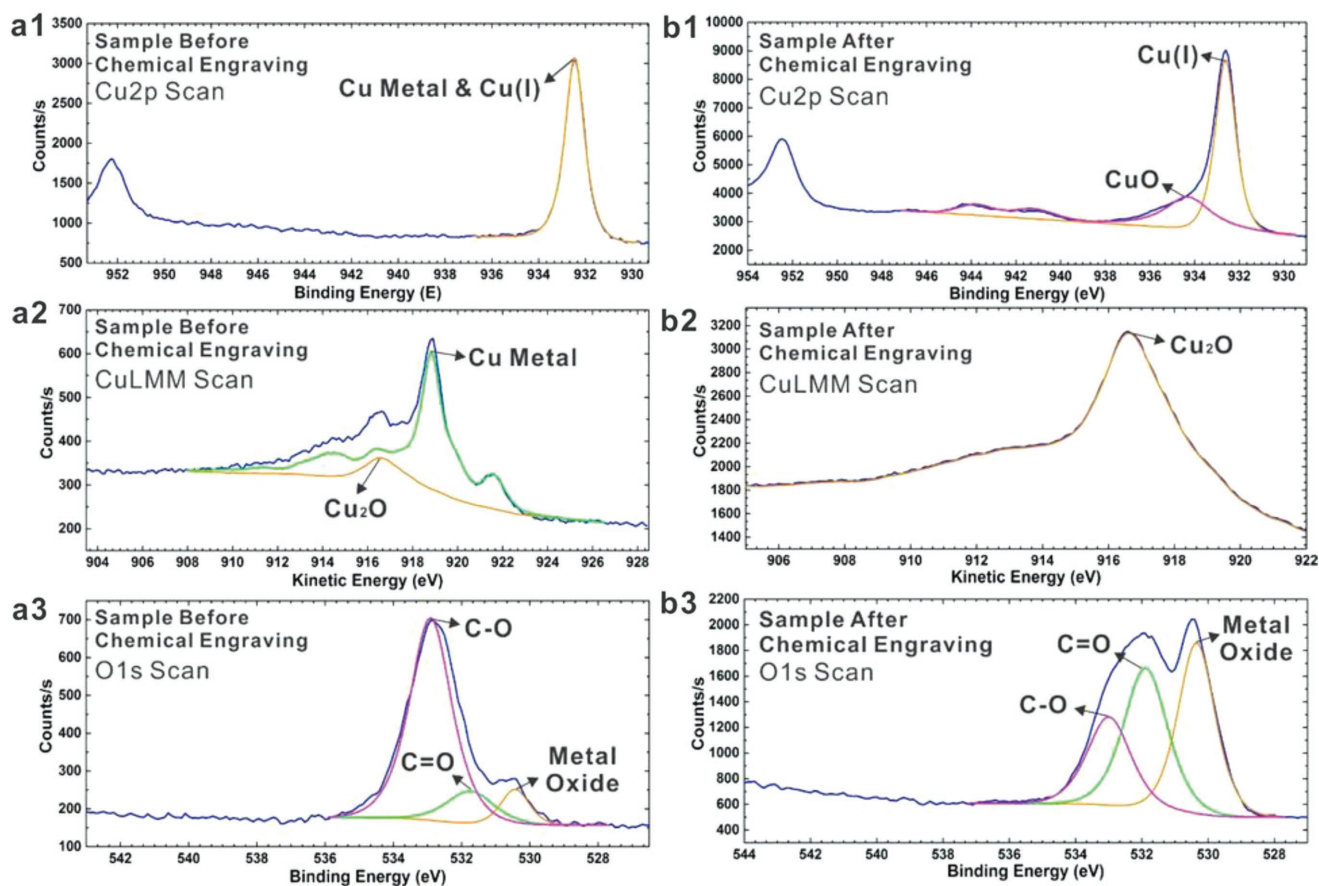

Figure 5. High-resolution XPS survey spectra of Cu 2p, Cu LMM and O 1s of samples a) before and b) after chemical engraving process.

1803600 (8 of 12)

**ADVANCED
SCIENCE NEWS**

www.advancedsciencenews.com

**ADVANCED
FUNCTIONAL
MATERIALS**

www.afm-journal.de

the two identified copper species were determined to be 23% Cu_2O and 77% Cu metal. This result indicates that the majority metal found on the surface of the electrode-prior to engraving-was Cu metal. The O 1s high-resolution spectrum is shown in Figure 5a3. As expected, a weak O1s metal oxide peak was found at 529.5 eV, further confirming the existence of Cu_2O on the surface. When characterizing the sample which had been chemically engraved, a similar process involving XPS was employed. As illustrated in Figure 5b1, the Cu $2p_{3/2}$ spectrum presents two peaks, one at 934.8 eV and the other at 932.7 eV. The peak at 934.8 eV can be ascribed to $Cu(OH)_2$, whilst the peak at 932.7 eV requires further analysis. The Cu LMM spectrum (Figure 5b2) of the engraved sample shows only one peak which well fits the Auger peak of Cu_2O at 916.8 eV. According to this, the peak at 932.7 eV from Cu $2p_{3/2}$ spectrum can be identified as peak from Cu_2O species and there is no Cu metal on the surface. By calculating the integral area of the two peaks from Cu $2p_{3/2}$, we found that the proportion of Cu $(OH)_2$ and Cu_2O was 39% and 61%, respectively. In the O1s spectrum presented in Figure 5b3, a strong peak at 529.4 eV was observed. This peak belongs to the metal oxide found on the surface of the sample and corresponds to the chemically engraved $Cu(OH)_2$ and Cu_2O. In brief, the XPS survey provides direct evidence that Cu(II) and Cu(I) species are both successfully introduced onto the surface through chemical engraving. It is acknowledged however, that XPS study can only reveal the insights into the surface layer (<5 nm thickness) and not further. To fully characterize the constituents of these samples, X-ray diffraction (XRD) was employed to better understand the composition and crystalline structure of the electrodes.

Figure 6 shows the XRD spectra of three different paper substrates. The first was taken just before metallization (top), the second was shortly after metallization by ELCD (middle), and the third sample was analyses after chemical engraving (bottom). The freshly metallized sample (middle) shows three clean and sharp peaks at 43.46°, 50.43°, and 74.25°, which coincide with the Cu metal crystal planes (111), (200), and (220), respectively (JCPDS Data 04–836). Interestingly, the XRD spectra is absent of any peaks pertaining to the presence of $Cu(OH)_2$, which contrasts that of the previous XPS survey

(Figure 5a). This finding implies that $Cu(OH)_2$ only exists on the very top surface of the sample, as there are no detectable quantities for the XRD machine. In the samples which had been chemically engraved for 48 h, the same three peaks observed in the freshly prepared sample are present but are accompanied by five others as well. The three familiar peaks appear to be of similar shape to those of the freshly metallized sample, but the peaks at 50.43° for Cu (200) and 74.25° for Cu (220) are considerably weaker, indicating that copper metal with such crystal structures may tend to get oxidized more easily during the chemical engraving process. A number of new but weaker peaks appear in the XRD spectrum; the peak at 23.8° corresponds to the (021) plane of $Cu(OH)_2$ crystal (JCPDS Data 80–0656), while the peak at 36.4° corresponds to the (111) plane of Cu_2O (JCPDS Data 05–0667) crystal. The three peaks clustered together at 35.7°, 38.7°, and 61.5° can be ascribed to the (11-1), (111), and (11-3) planes of the CuO crystal, respectively (JCPDS Data 48–1548). As observed in the fresh sample, different results were obtained in the XRD survey when compared to those of the XPS, which is again likely due to the much deeper detection depth of the XRD equipment. Based on the results obtained using XRD and XPS, we conclude that the electrochemically active materials generated by the engraving process are mainly Cu_xO, with small amounts of $Cu(OH)_2$ below the surface. It is also worth mentioning that the Cu(I) and Cu(II) ratio could be controlled by using different dehydration conditions (temperature, humidity, time, etc.) and could be optimized to further improve the performance of the SC.

2.6. Demonstration

One of the most attractive advantages of inkjet-printed SC is the strong ability of monolithically integration with other devices and its provision of aesthetic versatility. Using the fabrication method proposed in this work, the printed SCs can be readily connected in series or parallels without the use of extra metallic interconnects. To demonstrate the versatility of the proposed technique in real world applications, a flexible SCs array with four cells connected in series is fabricated on regular cellulose paper, which is able to provide a total voltage of ≈1.8 V (**Figure 7**a). The printed SCs adopted a planar design with 26 fingers crossing with each other. Each finger was 2 cm long, 400 µm wide, and was separated by a 400 µm gap in between. Charging ports (positive and negative) were printed on each side of the SCs array to accommodate the attachment of alligator clips, as shown in Figure 7a. Once charged, the two charging ports were each patched over by a piece of copper tape, closing the circuit with the single mounted LED. Note that the charging ports used in this example are arbitrary and could easily be replaced by a switch or a diode for the simple control of charging/discharging in real-world applications. The LED remained fully lit even when the device was bent and creased (see Figure 7c), reflecting excellent device flexibility. To demonstrate its capability of integrating with its intended application, a second pattern was created using the abbreviation of the authors' institute, "UWO" (see Figure 7d). The electronic art utilised four SCs (one in letter "U", two in letter "W", and one in letter "O") connected in series, which when combined were enough to
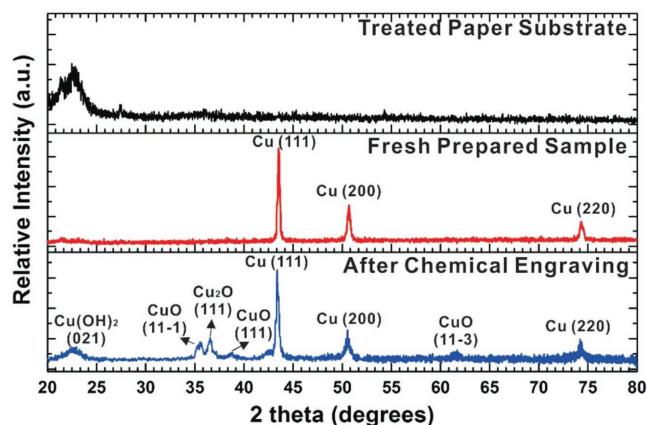

Figure 6. XRD spectra of treated paper substrate before metallization (top), sample after electroless copper deposition (middle), and sample after chemical engraving (bottom).
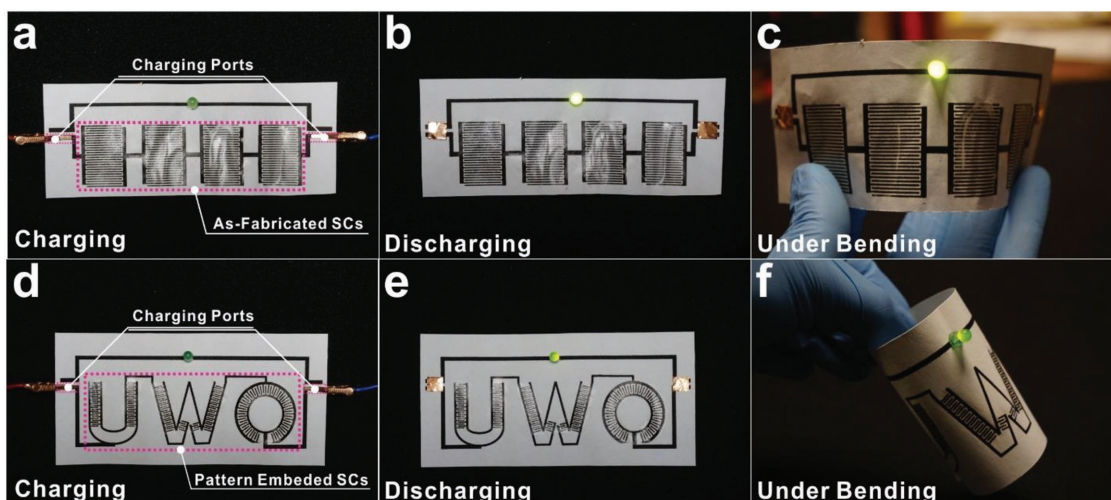
Figure 7. As-fabricated SCs with various form factors as object-tailored and monolithically integrated power sources. a) Charging and b) discharging of four SC cells connected in series. c) The as-fabricated device operating as intended in bend state. d) Charging and e) discharging of electronic art with four monolithically integrated SCs (one in letter "U", two in letter "W", and one in letter "O") connected in series. f) The device working properly when rolled into a cylinder.

power the LED lamp with ease (Figure 7e). To demonstrate the devices flexibility yet again, the device was rolled into a cylinder and showed changes to its performance as an LED-powering SC (Figure 7f). The above demonstration is evidence that the inkjet-printing-based technique proposed herein allows for the easy control of electrical properties (i.e., voltage and current) of the produced power sources through simple designing of the printing patterns. In addition to the facile control of the power source properties, the printed SCs can be seamlessly integrated into any printed circuits or even art work.

3. Conclusion

The demand for cheaper, more efficient, more reliable, safer, and environmentally sustainable alternatives to current energy storage systems is unquenchable. By exploiting the perfectly imperfect, overlooked properties of regular cellulose paper, we present a scalable method of fabricating low-cost, high-performance, all-solid-state SCs. The binder-free SCs capitalize on the randomly oriented cellulose fibers to house porous Cu_xO nanosheets, all using little more than a common inkjet printer. For the first time, we bridged the emerging printed electronics technology with a low-temperature chemical engraving method to construct nanostructured Cu_xO in situ on highly conductive current collectors. The new SCs can be seamlessly integrated to any printed circuit, artwork, or otherwise demonstrating their exceptional versatility and promise for applicability as a new generation of object-tailored power sources. The utilization of low-cost cellulose paper in tandem with electroless copper deposition and chemical engraving, has led to substantial improvements to the printed SCs all whilst significantly lowering their production cost. Moreover, with the involvement of inkjet printing, the printed SCs can be easily connected in series or parallel, allowing the user-customized control of the properties of the power sources. With little effort, the proposed method can be extended

to many other porous substrates with higher porosity to achieve better SC performance. Thus, we believe that the facile, low-cost, and large-scale method proposed here provides a promising way to produce a new class of monolithically integrated high-performance power sources, which are badly needed by the booming flexible/wearable electronics and IoT industries.

4. Experimental Section

Materials: Ethanol (anhydrous, denatured), 1,4-dioxane ($C_4H_8O_2$, 99.8%), Poly(4-vinyl pyridine) (P4VP, Mw ≈60 000), formaldehyde (HCHO, 36.5%–38% in water), anhydrous glycerol (C3H5(OH)3,99%), 2-propanol, silver nitrate ($AgNO_3$, 99%), copper sulfate pentahydrate ($CuSO_4 \cdot 5H_2O$, 98%), 2,2'-dipyridyl ($C_{10}H_8N_2O_2$, 98%), sodium hydroxide (NaOH, 97%), potassium sodium tartrate tetrahydrate ($C_4O_6H_4KNa \cdot 4H_2O$, 99%), ethylenediaminetetraacetic acid disodium salt dihydrate (EDTA·2Na, 98%), glycerol ($C_3H_8O_3$, 99%), hydrochloric acid (HCl, 37%), Poly(vinyl alcohol) (PVA, Mw ≈9000), potassium hydroxide (KOH, 90%), and potassium ferrocyanide (II) trihydrate ($K_4Fe(CN)_6 \cdot 3H_2O$, 98.5–102.0%) were purchased from Sigma–Aldrich (now Millipore-Sigma). SU-8 was provided by Kayaku Micro Chem. All chemicals were used as-received without any further purification or processing. Cellulose paper substrate was provided by Xerox.

Preparation of Coating Solution: P4VP (2.5 g), and SU-8 (2.5 g), were dissolved into ethanol (50 mL), and 1,4-dioxane (50 mL) respectively, to obtain 50 mg mL^{-1} transparent solution. The two solutions were then mixed at 1:1 volume ratio to obtain a transparent solution. The final solution contains 25 mg mL^{-1} P4VP and 25 mg mL^{-1} SU-8.

Surface Modification of Cellulose Paper: Untreated cellulose paper was immersed into the coating solution for 10 s. The paper was then drawn out of the solution in a constant, slow manner and allowed to dry in ambient room conditions for 5 min. Lastly, the coated paper was placed into an oven at 135 °C for 20 min for in situ cross-linking of P4VP and SU-8 molecules. Once cross-linked, the modified substrates were collected and stored in a cool, dry, and dark environment.

Preparation of Catalyst Ink for Inkjet Printing: A glycerol–water solution was prepared by mixing anhydrous glycerol and distilled water at a *V/V* ratio of 3:2. Silver nitrate was then added, followed by mixing in a VWR mixer for 3 min, to form a 40 mg mL^{-1} silver slat solution. The prepared

ink was degassed in a vacuum chamber at 2 psi for 1 h to remove dissolved gases and bubbles. The viscosity and surface tension of the final ink were 11.5 cp and 51.8 mN m^{-1}, respectively. These values fall within the optimum operating range for the Dimatix DMP-2800 Inkjet printer. A 0.2 µm nylon syringe filter was used to remove undesired particles from the ink prior to it being fed into the cartridge.

Inkjet Printing: The ink was filled into a cartridge mounted on a 10 pL piezo-electric drop-on-demand inkjet print head with 16 nozzles operating at the same time. The printer was set as following: drop spacing: 35 µm; meniscus vacuum: 3.5 inch of H$_2$O; print head temperature: 25 °C; jetting voltage 25.3 V. Printing was conducted at room temperature.

Electroless Deposition of Copper: An electroless copper plating bath consisting of CuSO$_4$·5H$_2$O (14 g L^{-1}), NaOH (12 g L^{-1}), potassium sodium tartrate (16 g L^{-1}), EDTA·2Na (20 g L^{-1}), HCHO (26 mL L^{-1}), 2,2'-dipyridyl (20 mg L^{-1}), and potassium ferrocyanide (10 mg L^{-1}) was prepared. Modified cellulose-fiber paper with printed silver nitrate patterns were immersed into the bath for 3 h. The temperature was kept at 35 °C to ensure high-speed deposition of the copper.

Chemical Engraving: Samples from the prior electroless deposition process were rinsed thoroughly under deionized water for 5 min. After rinsing, samples were immersed in 1 M HCl solution for 3 min, followed by another rinsing under deionized water for another 5 min. Sodium hydroxide was dissolved in deionized water to form a 40 mg mL^{-1} NaOH solution, which was preheated to 60 °C in a thermostatic water bath. Next, the pre-washed samples were put into the sodium hydroxide solution and were kept in a sealed contained with the temperature holding at 60 °C for 48 h. After that the samples were gently washed using deionized water and dried in a vacuum chamber for 3 hours at 85 °C.

Preparation of the Electrolyte and Device Assembly: Five grams of PVA was dissolved in 100 mL deionized water at 80 °C and was stirred for 8 h until a clear, transparent solution was formed. 3.5 g KOH was dissolved into a separate container containing 10 mL of deionized water, which was then added to the PVA solution dropwise under gentle stirring. The final solution was kept stirring for another 2 h until a homogeneous electrolyte was produced. After cooling down to room temperature, the electrolyte was deposited onto previously prepared planar electrodes using a pipette gun and was spread gently ensuring no contact was made with the surface of the electrodes. The samples were dried in air at room temperature for 8 h for further testing.

Characterization: FE-SEM images were taken using a LEO (Zeiss) 1540 FE-SEM. The viscosity of the ink was measured with a fully automatic HAAKE Viscotester 262. Surface tension of the ink was measured by VETUS BZY-3B fully automatic tensiometer. Sheet resistances were measured by a four-point probe station Lucas Labs S-302-4 (probe SP4), connected to a Keithley 2750 multimeter. CV and electrochemical impedance spectroscopy (EIS) tests were performed on a Bio-Logic multichannel potentiostat 3/Z (VMP3), with various scanning rates in a potential range of 0–0.6 V at room temperature. Galvanostatic charge/discharge and cyclic stability tests were carried out using an Arbin BT 2000 testing station with a current density of 20 mA cm^{-2} and a voltage window of 0–0.6 V. All electrochemical tests were configured as a two-electrode system. XRD analysis was done using a Rigaku Ultima-IV XRD goniometer, and XPS was performed using a Kratos AXIS Ultra spectrometer.

Acknowledgements

Conflict of Interest

The authors declare no conflict of interest.

[1] J. Gubbi, R. Buyya, S. Marusic, M. Palaniswami, *Future Gener. Comput. Syst.* **2013**, *29*, 1645.
[2] J. S. Heo, J. Eom, Y. H. Kim, S. K. Park, *Small* **2017**, *14*, 1703034.
[3] M. Sugathan, M. D. Hendry, *Int. J. Technol. Diffus.* **2017**, *8*, 57.
[4] M. Moussa, M. F. El-Kady, Z. Zhao, P. Majewski, J. Ma, *Nanotechnology* **2016**, *27*, 442001.
[5] H. Chen, T. N. Cong, W. Yang, C. Tan, Y. Li, Y. Ding, *Prog. Nat. Sci.* **2009**, *19*, 291.
[6] Y. Ko, M. Kwon, W. K. Bae, B. Lee, S. W. Lee, J. Cho, *Nat. Commun.* **2017**, *8*, 536.
[7] P. Simon, Y. Gogotsi, B. Dunn, *Science* **2014**, *343*, 1210.
[8] P. Simon, Y. Gogotsi, *Nat. Mater.* **2008**, *7*, 845.
[9] P. Yang, W. Mai, *Nano Energy* **2014**, *8*, 274.
[10] Z. Yu, B. Duong, D. Abbitt, J. Thomas, *Adv. Mater.* **2013**, *25*, 3302.
[11] T. M. Dinh, A. Achour, S. Vizireanu, G. Dinescu, L. Nistor, K. Armstrong, D. Guay, D. Pech, *Nano Energy* **2014**, *10*, 288.
[12] W. Wei, X. Cui, W. Chen, D. G. Ivey, *Chem. Soc. Rev.* **2011**, *40*, 1697.
[13] X. Lu, D. Zheng, T. Zhai, Z. Liu, Y. Huang, S. Xie, Y. Tong, *Energ. Environ. Sci.* **2011**, *4*, 2915.
[14] T. Y. Wei, C. H. Chen, H. C. Chien, S. Y. Lu, C. C. Hu, *Adv. Mater.* **2010**, *22*, 347.
[15] X. Wang, C. Yan, A. Sumboja, P. S. Lee, *Nano Energy* **2014**, *3*, 119.
[16] R. Rakhi, W. Chen, D. Cha, H. N. Alshareef, *Nano Lett.* **2012**, *12*, 2559.
[17] D. Choi, G. E. Blomgren, P. N. Kumta, *Adv. Mater.* **2006**, *18*, 1178.
[18] K. Chen, D. Xue, *ACS Appl. Mater. Interfaces* **2016**, *8*, 29522.
[19] M. Momeni, Z. Nazari, A. Kazempour, M. Hakimiyan, S. Mirhoseini, *Surf. Eng.* **2014**, *30*, 775.
[20] G. Wang, L. Zhang, J. Zhang, *Chem. Soc. Rev.* **2012**, *41*, 797.
[21] K.-H. Choi, J. Yoo, C. K. Lee, S.-Y. Lee, *Energ. Environ. Sci.* **2016**, *9*, 2812.
[22] Y. He, W. Chen, X. Li, Z. Zhang, J. Fu, C. Zhao, E. Xie, *ACS Nano* **2012**, *7*, 174.
[23] S. Lawes, Q. Sun, A. Lushington, B. Xiao, Y. Liu, X. Sun, *Nano Energy* **2017**, *36*, 313.
[24] S. Lawes, A. Riese, Q. Sun, N. Cheng, X. Sun, *Carbon* **2015**, *92*, 150.
[25] X. Wang, X. Lu, B. Liu, D. Chen, Y. Tong, G. Shen, *Adv. Mater.* **2014**, *26*, 4763.
[26] B. C. Kim, J. Y. Hong, G. G. Wallace, H. S. Park, *Adv. Energy Mater.* **2015**, 5.
[27] Z. Liu, Z. S. Wu, S. Yang, R. Dong, X. Feng, K. Müllen, *Adv. Mater.* **2016**, *28*, 2217.
[28] H. Zhang, Y. Qiao, Z. Lu, *ACS Appl. Mater. Interfaces* **2016**, *8*, 32317.
[29] C. Zhou, Y. Zhang, Y. Li, J. Liu, *Nano Lett.* **2013**, *13*, 2078.
[30] C. K. Chan, H. Peng, G. Liu, K. McIlwrath, X. F. Zhang, R. A. Huggins, Y. Cui, *Nat. Nanotechnol.* **2008**, *3*, 31.
[31] H. Zhang, X. Yu, P. V. Braun, *Nat. Nanotechnol.* **2011**, *6*, 277.
[32] R. R. Salunkhe, K. Jang, H. Yu, S. Yu, T. Ganesh, S.-H. Han, H. Ahn, *J. Alloy Compd.* **2011**, *509*, 6677.
[33] Z. Tang, C. h. Tang, H. Gong, *Adv. Funct. Mater.* **2012**, *22*, 1272.
[34] S. Yuan, X. l. Huang, D. l. Ma, H. g. Wang, F. z. Meng, X. b. Zhang, *Adv. Mater.* **2014**, *26*, 2273.
[35] S. Shinde, D. Dubal, G. Ghodake, V. Fulari, *RSC Adv.* **2015**, *5*, 4443.

[36] D. Dubal, D. Dhawale, R. Salunkhe, V. Jamdade, C. Lokhande, *J. Alloy Compd.* **2010**, *492*, 26.

[37] A. Lamberti, M. Fontana, S. Bianco, E. Tresso, *Int. J. Hydrogen Energy* **2016**, *41*, 11700.

[38] Z. Endut, M. Hamdi, W. Basirun, *Thin Solid Films* **2013**, *528*, 213.

[39] G. O. Mallory, J. B. Hajdu, *Electroless Plating: Fundamentals and Applications*, William Andrew, **1990**.

[40] T. Zhang, M. Hu, Y. Liu, Q. Guo, X. Wang, W. Zhang, W. Lau, J. Yang, *Appl. Phys. Lett.* **2016**, *108*, 103501.

[41] T. Zhang, X. Cai, J. Liu, M. Hu, Q. Guo, J. Yang, *Adv. Sustainable Syst.* **2017**, *1*, 1700062.

[42] T. Y. Zhang, X. L. Wang, T. J. Li, Q. Q. Guo, J. Yang, *J. Mater. Chem. C* **2014**, *2*, 286.

[43] W. Wang, E. Kang, K. Neoh, *Appl. Surf. Sci.* **2002**, *199*, 52.

[44] J. B. You, S. Y. Kim, Y. J. Park, Y. G. Ko, S. G. Im, *Langmuir* **2014**, *30*, 916.

[45] X. Wen, W. Zhang, S. Yang, Z. R. Dai, Z. L. Wang, *Nano Lett.* **2002**, *2*, 1397.

[46] P. Hartman, W. G. Perdok, *Acta Crystallographica* **1955**, *8*, 49.

[47] W. Zhang, X. Wen, S. Yang, *Inorg. Chem.* **2003**, *42*, 5005.

[48] S. X. M. Boerrigter, H. M. Cuppen, R. I. Ristic, J. N. Sherwood, P. Bennema, H. Meekes, *Cryst. Growth. Des.* **2002**, *2*, 357.

[49] T. Zhang, E. Asher, J. Yang, *Adv. Mater. Technol.* **2018**, *3*, 1700346.